ROYAL SOCIETY OF CHEMISTRY

PAPER

MnO nanoparticles with cationic vacancies and discrepant crystallinity dispersed into porous carbon for Li-ion capacitors†

Chaofeng Liu,[a] Changkun Zhang,[a] Huanqiao Song,[a] Xihui Nan,[a] Haoyu Fu[a] and Guozhong Cao*[ab]

MnO nanoparticles with cationic vacancies and discrepant crystallinity were prepared through a one-step hydrothermal synthesis followed by calcination at different temperatures. Glucose was used as both a reducing agent to introduce cationic vacancies with a content of ~5.5% into MnO nanocrystals, and a carbon source to encapsulate MnO nanocrystals in a three dimensional porous framework. Cationic vacancies benefit phase transition in a conversion reaction, and together with a low degree of crystallinity, may also provide more void spaces for ion diffusion (3.37×10^{-13} cm^2 s^{-1}). Three dimensional porous carbon with a pore volume of 0.27 cm^3 g^{-1} demonstrated a high electrical conductivity of 6.25 S cm^{-1} and offered fast pathways for charge transfer and penetration of the electrolyte. Such a synergistic structure endowed MnO with excellent electrochemical properties including a considerably enhanced capacity of 650 mA h g^{-1} at a current density of 1000 mA g^{-1}. Li ion capacitors based on such a MnO anode and activated carbon cathode achieved the maximum energy density of 220 W h kg^{-1}, and the capacitance retention was 95.3% after 3600 cycles at a rate of 5000 mA g^{-1}.

Introduction

The supply and management of energy are, more than ever, at the center of our daily concerns because of the fossil fuels-based energy mode-induced serious environmental issues such as greenhouse effects caused by the emission of carbon dioxide from fuel combustion.[1,2] A more imperative challenge lies ahead because the population explosion in the following 30 years would double the consumption of energy from 14 TW to 28 TW[3]. Renewable energy, such as solar, wind and biomass, provides reliable alternative energy candidates for coping with such increasing socioeconomic pressures.[4,5] However, the intermittent character of these renewable energy demands efficient solutions and technologies for energy conversion and storage. Currently, secondary batteries and supercapacitors are two reliable and safe candidates for energy storage that are especially widely applicable in smart portable apparatus.[6,7] Both technologies offer advantages, but they both suffer from disadvantages in their own aspects. Secondary, or rechargeable, batteries depend on redox

reactions at the interface between the electrode material and the electrolyte accompanied with solid state mass and charge diffusion and phase transition; they supply a high energy density but are limited with their power output.[8,9] Supercapacitors, on the other hand, rely on the formation of an electric double layer at the interfaces between the conductive electrode and the electrolyte without involving solid state mass diffusion; the instantaneous charge adsorption/desorption endows ultrahigh power density but with a low energy density.[10–12] With a promise to synergistically combine the advantages of two energy storage technologies, hybrid electrochemical systems, such as Li-ion capacitors, have attracted significant attention in the research community. In particular, Li-ion capacitors build on one power-type electrode with another energy-type electrode for integrating the merits from batteries and supercapacitors.[13,14] Similar to lithium-ion batteries and supercapacitors, the specific capacity of the electrode and the working voltage window determine the energy density of Li-ion capacitors; thus, it is essential to enhance the specific capacity of electrode materials and choose suitable electrodes with appropriate working potentials for the fabrication of a high performance Li-ion capacitor. Anodes with low electrochemical potentials are beneficial for obtaining a large working voltage in full batteries or capacitors. If these anodes have large capacities as well, high energy density capacitors can be readily assembled. Manganese monoxide, an important member in the

[a]Beijing Institute of Nanoenergy and Nanosystems, Chinese Academy of Sciences, Beijing, 100083, China. E-mail: gzcao@u.washington.edu

[b]Department of Materials Science and Engineering, University of Washington, Seattle, Washington, 98195, USA

† Electronic supplementary information (ESI) available: Additional figures depicting experiment results. See DOI: 10.1039/c5ta10002j

manganese family, possesses a low electrochemical potential around 0.5 V $vs.$ Li/Li$^+$, which avoids electrolyte decomposition without sacrificing the voltage window for the capacitors. In addition, it has a large theoretical capacity of 760 mA h g^{-1}, which is double than that of graphite.[15,16] Many efforts have been devoted to the improvement of the cyclic stability and rate capability of MnO through the design and fabrication of novel microstructures or composites with carbonaceous materials.[16–20] For example, MnO nanowire/graphene displays excellent electrochemical performances because graphene can capture the collapsed MnO particles for avoiding the separation between active materials and the collector.[20] Peapod-like MnO/C provides an internal void space to suffer and inhibit the dissolution, aggregation and volumetric expansion of MnO during the conversion reaction.[16] However, few studies have focused on the effect of crystallinity on the electrochemical performances in MnO. Some reports have demonstrated that the inferior crystallinity endows excellent properties in other compounds[21–25] due to more space or sites that can be utilized for ion diffusion or storage. Besides, defects, such as vacancies, also play a pivotal role in improving the performance of electrode materials because they can provide nucleating sites at the initial phase transition.[26,27] Introduction of defects in the crystal lattice was achieved through introducing appropriate dopants or by thermal treatment in reduction/oxidation gases.[28–30] In the present study, MnO nanoparticles dispersed in porous carbon with cation vacancies and a low degree of crystallinity were synthesized using a one-step hydrothermal method followed with heat treatment at elevated temperatures between 600 and 900 °C. In contrast to most of the studies published in the literature that focus on the fabrication and impact of nanostructures and micro-structures, the presence and amount of cationic vacancies, the crystallinity of the samples annealed at different temperatures and their electrochemical properties were studied systematically in both half cells and full Li-ion capacitors. The influence of cationic vacancies and low degrees of crystallinity on the electrochemical properties and the electrical energy storage performance of Li-ion capacitors have been elaborated and discussed.

Experimental section

Synthesis

A certain amount of glucose and 5.88 g of manganese acetate tetrahydrate were dissolved in 70 ml de-ionized water with continuous magnetic stirring to obtain a transparent solution. Then, 1.58 g of KMnO$_4$ was directly added to the solution and stirred for 30 min to obtain a brown mixture. The mixture was placed in a Teflon-lined stainless steel autoclave and heated to 180 °C for 30 min. The product was washed by DI water and alcohol several times and dried at 80 °C for 4 h. Finally, the powder was calcined at different temperatures for 2 h under Ar flowing at 100 standard cubic centimeters per minute (sccm). The samples were calcined at different temperatures for studying the effect of crystallinity on electrochemical performance.

Structural characterization

The crystalline structure and micro-structure of the samples were studied on a X' Pert^3 diffractometer (PANalytical, Netherlands), using a Cu-Kα radiation source ($\lambda = 1.54056$ Å) with a step size of 0.013°, and a cold field emission scanning electron microscope (FESEM, HITACHI SU8200) at 5 kV and 10 μA, respectively. The lattice image was observed through high resolution transmission microscopy (HRTEM, FEI/Tecnai G2 F20 S-TWIN TMP) with an accelerating voltage of 200 kV. Raman spectra were obtained at resolution of 0.65 cm^{-1} with a Horiba JOBIN YVON Raman system (LabRAM HR Evolution) using an argon ion laser (532 nm) as the excitation source. The total surface area was investigated using nitrogen sorption analyses via a Micromeritics surface area and porosity analyzer (ASAP 2020 HD88, USA). The degas condition was set to 250 °C with 4 h under a vacuum of 500 μmHg ($\sim$0.67 mbar), all the adsorption–desorption measurements were conducted at liquid nitrogen temperature. Barrett–Joyner–Halenda (BJH) method was adopted to calculate the mesopore surface area, pore volume and pore diameter, whereas the specific surface area and the pore volume of micropores were calculated using the t-method. A TGA/DTA instrument (Mettler-Toledo STAR system, TGA/SDTA) was used to study the pyrolyzing reaction in the spindle precursor under Ar gas flowing at the rate of 50 ml min^{-1}, and the carbon content of the calcined samples were detected under oxygen flowing at the rate of 50 ml min^{-1}. Electrical conductivity of the samples was measured using a direct current four-probe technique (ST-2722 semiconductor resistivity of the powder tester, Suzhou Jingge Electronic. Co., Ltd.) at a pressure of 4 MPa.

Capacitor fabrication and electrochemical characterization

The electrochemical performances of all the samples were investigated using 2032 coin cells. To prepare the working electrode, the slurry containing a mixture of active materials (MnO), carbon black and poly-(vinyl difluoride) (PVDF) at a weight ratio of 80 : 10 : 10 was bladed onto a Cu foil and then subjected to a thermal treatment at 120 °C with 12 h in vacuum. The mass loading of the active material on each electrode disk was 1.0–1.5 mg cm^{-2}. The electrolyte was 1 M LiPF$_6$ in a 1 : 1 : 1 (vol%) mixture of ethylene carbonate, dimethyl carbonate and diethyl carbonate, and a polypropylene film (Celgard 2400) was used as the separator. Li-ion capacitors were fabricated with commercial activated carbon employed as cathodes and MnO electrodes as anodes. The specific surface area of the commercial activated carbon approximates to 1800 m^2 g^{-1} as studied in our previous work.[31] The fabrication of cathodes was similar with anodes but on an Al foil. Half cells were also assembled and lithium foil was used as the counter electrode for investigating the electrochemical properties of anode materials. All the cells were assembled in an argon-filled glovebox in which both the content of oxygen and water were below 1 ppm.

Galvanostatic charge–discharge tests of all the cells were carried out on a Land CT2001A system (Wuhan, China) with various current densities. The operating voltage window for spindle MnO, activated carbon half cells and Li-ion capacitors

were 0.01–2.50 V (*vs.* Li/Li⁺), 2.00–4.50 V (*vs.* Li/Li⁺) and 0.10–4.00 V (spindle MnO//AC), respectively. Cyclic voltammograms (CVs) were obtained on a Solartron SI 1287 at the scanning rate of of 0.1 mV s⁻¹ for characterizing the redox reaction of electrode materials during the charge/discharge process. Electrochemical impedance spectroscopy (EIS) was performed at 3.0 V using the Solartron 1287A in conjunction with a Solartron 1260A impedance analyzer over the frequency range from 100 kHz to 0.1 Hz and the AC amplitude was 10.0 mV. The current densities applied to the half cells were calculated on the mass of active materials of electrodes and Li-ion capacitors were determined based on total mass of active materials on both electrodes. All the electrochemical measurements were carried out at room temperature. The specific energy and specific power values of Li-ion capacitors were calculated as follows:

$$P = I \times \Delta V/m$$

$$E = P \times t$$

$$\Delta V = V_{max} - V_{min}$$

where C is the discharge capacitance and t is the discharge time, V_{max} is the potential at the beginning of discharge after the IR drop, and V_{min} is the potential at the end of discharge.

Results and discussion

Phase compositions of the samples were detected by a XRD diffractometer with a step size of 0.013° and a time per step of 150 s to maintain the comparability. Fig. 1a shows the XRD patterns of the samples calcined at various temperatures and all the XRD peaks can be well indexed to MnO ($Fm\bar{3}m$, PDF 07-0230), distinguishable from the solvothermal product of $MnCO_3$ (Fig. S1a†), indicating that $MnCO_3$ was completely decomposed at the calcination temperature. It is worth noting that the characteristic peaks of XRD patterns become increasingly sharper with increasing calcination temperature, as shown in Fig. 1a, indicating the increased degree of crystallinity in MnO. Fig. 1b exhibits the tendency of full width at half maximum (FWHM) and intensities of (111) peak as a function of calcination temperature; the higher the calcination temperature, the narrower FWHM. A monotonic change in the FWHM and the peak intensity was found to be related to the calcination temperature. The narrower FWHM and higher intensity indicate that the sample has the higher degree of crystallinity.[32] Obviously, a sharp increase in the values appears when the samples are annealed at 800 °C and 900 °C. At the same time, the aromatized glucose produced in the synthesis process (Fig. S1b†) was carbonized during the calcination process. Raman spectra were used to analyze the degree of graphitization of the carbon in the calcined samples (Fig. S2a†). According to the Raman spectra of carbon materials, the D band stems from a double resonance process involving a phonon and a defect, and the G band corresponds to in-plane vibrations and has E_{2g} symmetry.[33] With the increase of calcination temperature, the intensities of D-and G-band enhanced gradually and the I_D/I_G

ratios decreased from 0.95 to 0.84, demonstrating that the carbon derived from aromatized glucose has a high degree of graphitization.[34] Fig. S2b† shows that the electrical conductivity was enhanced by two orders of magnitude as calcination temperature increased from 600 to 700 °C, but a further increase in calcination temperature did not improve the electrical conductivity considerably. In addition, the nitrogen sorption isotherms (Fig. S3a†) show that the total surface area of all the calcined sample was found to exceed 200.0 m² g⁻¹, higher than the value of 29.1 m² g⁻¹ for the samples before calcination (Fig. S3b†). The difference in surface area before and after calcination demonstrates that the pyrolysis of aromatized glucose created additional pores,[35,36] and the pore size distribution peaks appeared at ~4 nm (Fig. S3c†). Besides, CO_2 liberated from the pyrolysis of $MnCO_3$ may partially contribute to the formation of pores in the carbon matrix. Table 1 compares the surface area, pore volume and pore size of all the samples treated at various calcination temperatures and reveals that both mesopore surface area and pore volume sharply increased with increased calcination temperature. However, the micropore surface area decreased with increased calcination temperature. In addition, carbonization causes the densification of the carbon matrix; as a result, the average pore size slightly decreases from 4.77 to 4.27 nm with the elevation of calcination temperatures, as listed in Table 1. Based on the abovementioned contexts, it was found that the samples annealed at 600 and 900 °C possess the largest difference in the degree of crystallinity and electrical conductivity. Therefore, the following analyses and discussion will be focused mainly on both of them.

To discern the valence state of cationic ions in both samples, X-ray photoelectron spectra (XPS) were obtained (Fig. 1c and d) and the separation of 11.6 eV between Mn 2p₁/₂ and Mn 2p₃/₂ agreed well with the characteristic of MnO,[37,38] corroborating with the XRD results in Fig. 1a. The Mn 2p₃/₂ peak can be fitted by three Gaussian functions located at 640.8, 641.8 and 644.2 eV, respectively. The peak at 642.2 eV stems from Mn^{3+} and the other two peaks correspond to Mn^{2+}.[39,40] The content of Mn^{3+} was estimated utilizing the simulative peak areas and found to be 10.8% and 10.3% in the samples annealed at 600 °C and 900 °C, respectively. The presence of trivalent manganese ions indicated the incomplete reduction of Mn^{7+} to Mn^{2+} and further suggested the presence of the cationic vacancies created in the MnO lattice to maintain the required electro-neutrality. At the same time, a lower content of Mn^{3+} in the sample annealed at 900 °C demonstrated that carbon partially reduced the high valence state Mn^{3+} to Mn^{2+}. Noticeably, Mn^{3+} is difficult to obtain from the oxidation of Mn^{2+} in air, because Mn^{2+} has the lowest Gibbs free energy and the most stable electronic configuration ($3d^5$) at the outer orbital (Fig. S4†).[41] Besides, carbon coating acts as an inhibiting layer to protect the surface of MnO from making contact with a strong oxidant. In addition, SEM images show that both samples have a spindle-like shape and that the sample annealed at 600 °C (Fig. S5a†) exhibits bigger sizes in length, or width, than that annealed at 900 °C (Fig. S5b†), implying the higher calcination temperature resulted in a compact carbon matrix with a small shape volume. The
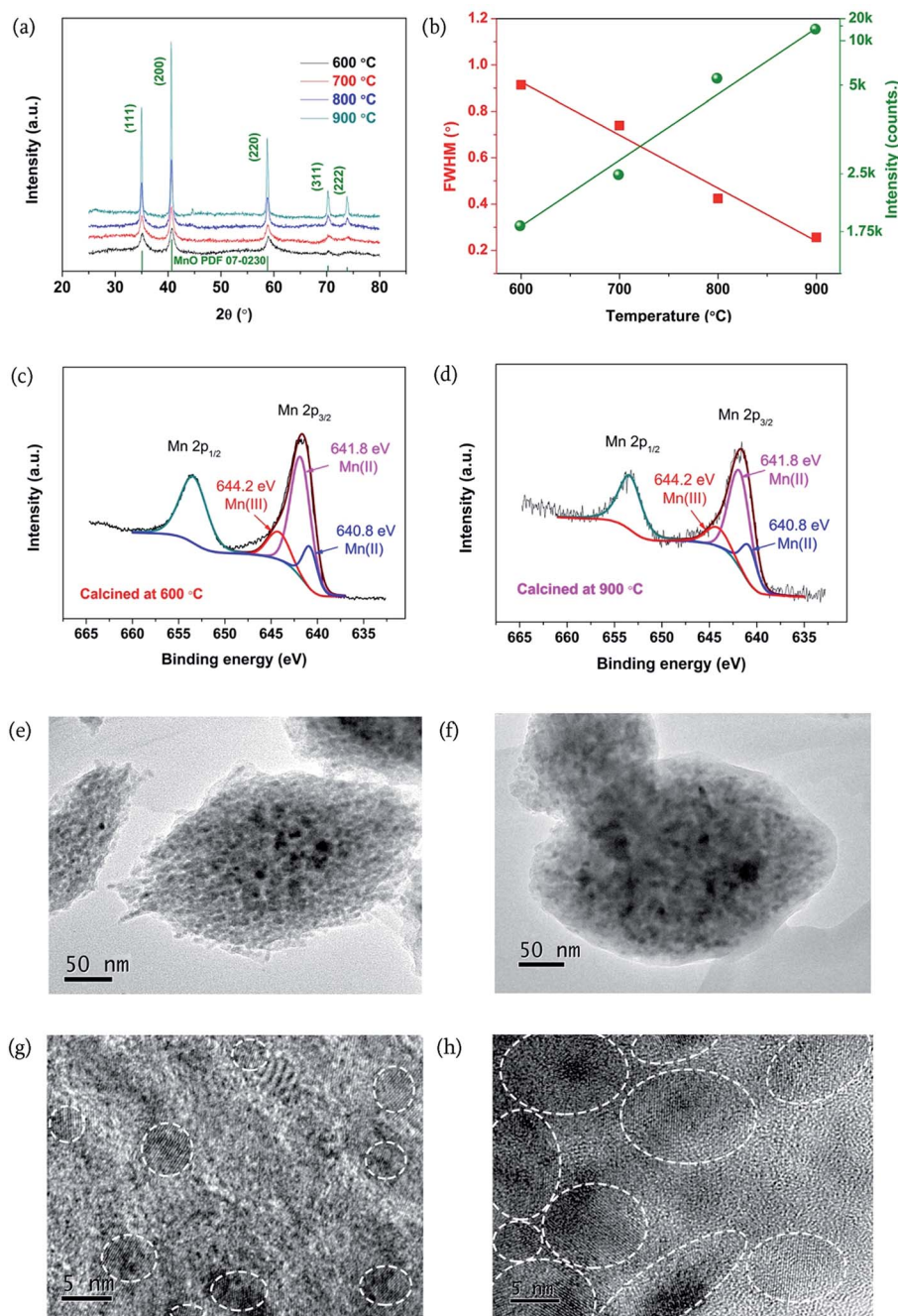
Fig. 1 (a) XRD patterns of the resulting samples from different calcination temperatures. (b) FWHMs and intensities of the (111) peak in samples from (a). The enhanced intensity and decreased FWHM demonstrated that the higher degree of crystallinity in samples was obtained with the increase of calcination temperatures. XPS spectra of samples after annealing at (c) 600 °C and (d) 900 °C. The separation between the Mn $2p_{1/2}$ and Mn $2p_{3/2}$ is 11.6 eV, which agrees with the characteristics of MnO in the two samples. The simulative peak areas from Gaussian functions can be used to evaluate the content of Mn^{3+} in the crystal lattice of MnO, and the results are 10.8% and 10.3% for the samples annealed at 600 and 900 °C, respectively. TEM images of the sample annealed at 600 °C (e) and 900 °C (f) show the difference of surface states in the two samples, revealing that the higher temperature benefits mass diffusion for lowering the surface energy. HRTEM images of the samples annealed at 600 °C (g) and 900 °C (h). The sample annealed at 900 °C has a higher degree of crystallinity and expanded crystallite zones compared with those in the sample annealed at 600 °C, which agree with the XRD results. The crystallite zones are marked by white-dashed circles.

details of the single spindles were investigated through TEM. Sample annealed at 600 °C consisted of numerous nanoparticles with a size of several nanometers, and some thorn-like matrix stood on the surface of the spindle (Fig. 1e). However, the spindle of the sample annealed at 900 °C was also made up of nanoparticles with small sizes and it has a smooth surface and no salient points can be observed on the external surface (Fig. 1f). The smoothness difference in the two samples reveals

Table 1 BET surface area, pore volume, average pore size and particle size of samples calcined at different temperatures

Sample ID	S_{Total} (m^2 g^{-1})	S_{Meso} (m^2 g^{-1})	S_{Micro} (m^2 g^{-1})	Pore volume (cm^3 g^{-1})	Average pore size (nm)
Before calcination	29.1	14.6	14.5	0.06	16.96
600 °C	243.1	178.0	65.1	0.24	4.77
700 °C	245.0	179.8	65.2	0.24	4.50
800 °C	245.0	212.0	33.0	0.25	4.37
900 °C	265.5	240.9	24.6	0.27	4.27

that higher temperatures benefit the mass diffusion to obtain lower energy level surfaces.[42] More importantly, HRTEM provides a view of the tiny details in the two samples and it could be found that the sample annealed at 600 °C contains crystallite zones with a size of ~6 nm (Fig. 1g); the amorphous zone would be comprised of carbon or/and manganese oxide. However, the sample annealed at 900 °C (Fig. 1h) has expanded crystallite zones with a bigger size of ~8 nm. It is noticeable that the crystalline sizes calculated by the Scherer equation on (111) peaks in XRD patterns are 14.3 and 31.7 nm for the samples annealed at 600 and 900 °C, respectively, which are larger than the sizes of the observed crystalline zones under HRTEM. Two possibilities can explain this difference. On the one hand, the calculations in XRD are affected by some factors, such as strain and stress. On the other hand, HRTEM observed a local zone of the sample rather than the average value in the whole sample. Therefore, the difference between XRD and HRTEM is understandable and acceptable. Besides, the number of crystallite zones is also increased as marked by white-dashed circles in Fig. 1g and h. This increased crystallinity from 600 to 900 °C agrees with the results of XRD shown in Fig. 1a and b. The apparent lattice fringes with inter-planar spacing of 2.57 Å or 2.22 Å, observed clearly in the HRTEM images of both samples, are in good accordance with the planar distances between the (111) or (200) planes of MnO, respectively. It is worth noting that some crystallite zones are connected with the same crystallographic orientation as observed in a mesocrystal,[43–45] and some zones prefer the other crystallographic orientation, leading to the single spindle without a unique orientation. The possibility to this difference may derive from aromatized glucose that supplies a steric effect to hinder the rotation and rearrangement of precursor nanoparticles for an ordering attachment or homoepitaxial aggregation. Apart from the steric effect, aromatized glucose also supplies a porous conductive network for the MnO nanoparticles. Assuming that the crystallinity zone is a spherical body, the theoretical surface area can be evaluated on the observed size and the MnO density, and the data should be 98 m^2 g^{-1}, which is lower than the measured results in Table 1. The difference may originate from the porous carbon that was created by the pyrolyzed glucose.[35,36,46] Besides, TG measurements demonstrate that both the samples have similar carbon content (Fig. S6†), and energy dispersive X-ray spectroscopy (EDX) results reveal the anticipated homogenous distribution of all the constituent elements (Fig. S7†), further supporting the homogeneous dispersion of nanosized MnO crystals in porous carbon. Porous carbon is known to facilitate the penetration of electrolyte and provide electron pathways around the electroactive crystallites.[35,36]

Cyclic voltammograms (CV) of sample annealed at 600 °C were collected for 3 cycles at a scanning rate of 0.1 mV s^{-1} within the voltage range of 0.01–2.50 V vs. Li/Li$^+$ at room temperature and the measured CV curves are shown in Fig. 2a. In the first cathodic scan, a weak peak at 0.75 V disappeared in the subsequent cycles, which corresponds to the formation of an SEI layer. A strong peak at 0.3 V corresponds to the conversion reaction, where MnO reacts with lithium ions to form Mn and Li$_2$O.[47] In the anodic scan direction, the peak at 1.22 V stems from the oxidation of Mn and decomposition of Li$_2$O. All the characteristics agree well with previously reported studies.[18,20,48] The CV curve in the third scan is almost identical to that of the second one, implying excellent reversibility. To further explore the capacitive contribution to the current response, the response can be described by two separate components, a surface capacitive effect (k_1v) and a diffusion-controlled process ($k_1v^{1/2}$):[49]

$$i(V) = k_1v + k_2v^{1/2} \tag{1}$$

For analytical purposes, the eqn (1) slightly changes to

$$i(V)/v^{1/2} = k_1v^{1/2} + k_2 \tag{2}$$

where k_1 and k_2 at the different potentials can be determined. Fig. 2b shows the CV profiles of sample 600 °C at the scan rate of 0.5 mV s^{-1} and the capacitive current (shaded area) of the sample as compared with the total measured current. The pseudo-capacitive contribution is ~40% as calculated from the area ratio. In addition, electrochemical impedance spectra (EIS) were collected at 3.0 V to compare the resistances to electron and ion migration in the two samples (Fig. 2c). The curve contains a semicircle for high frequencies and is followed by a straight line at low frequencies. An equivalent circuit is shown in the inset of Fig. 2c, which was used to discern the values of resistances, where R_s, R_f, R_{ct}, CPE and Z_W represent the resistance of the electrolyte, the resistance of the SEI film and charge transfer resistance, the double layer capacitance and the Warburg resistance, respectively. The arcs at high frequencies are assigned to the charge transfer resistance of electrode materials.[47] Remarkably, the value of the sample annealed at 900 °C (227 Ω) is smaller than that of sample annealed at 600 °C (323
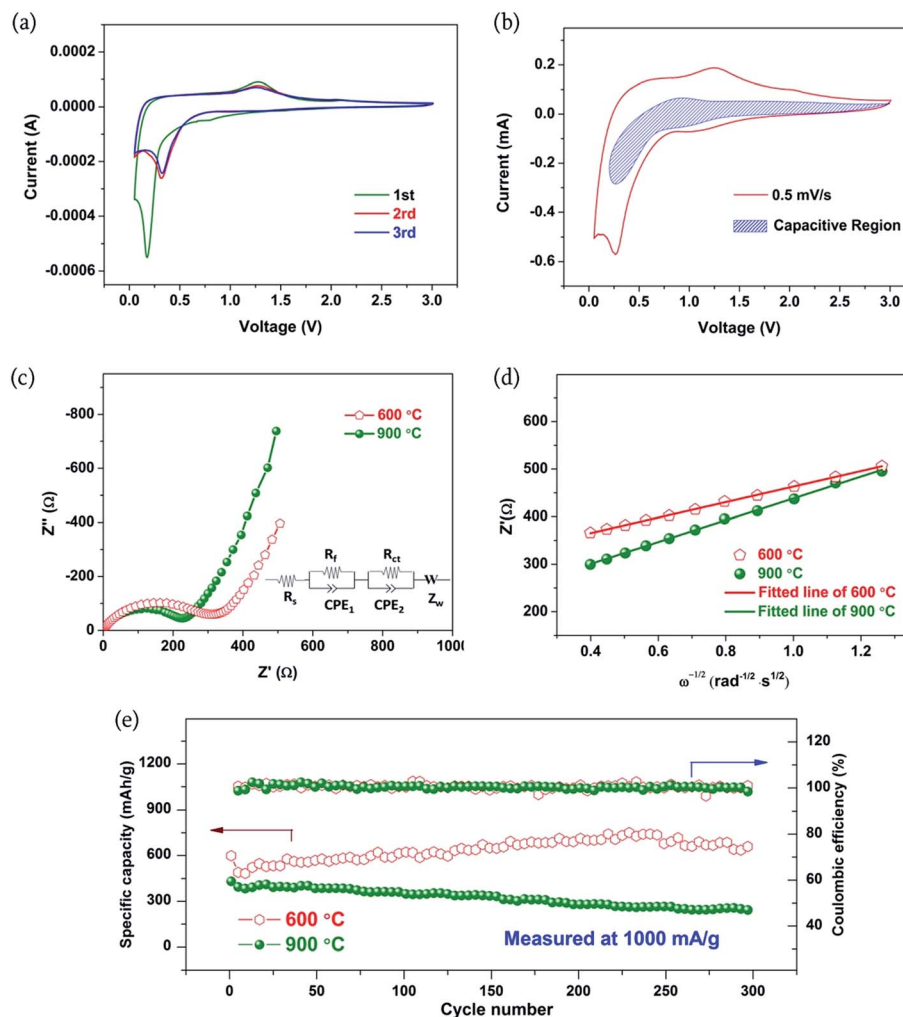
Fig. 2 (a) CV curves of the sample annealed at 600 °C, collected at a scanning rate of 0.1 mV s^{-1} within the voltage range of 0.01–3.00 V. (b) Voltammetric response for the sample annealed at 600 °C electrode at a sweep rate of 0.5 mV s^{-1}. The capacitive contribution to the total current is shown by the shaded region. (c) EIS spectra of the samples annealed at 600 and 900 °C. The sample annealed at 900 °C has a lower charge transfer resistance, which can be supported by the electrical conductivities shown in Fig. S2b.† (d) The relationship between the real parts of impedance and frequencies. The slopes can be used to calculate the Li-ion diffusion coefficient in the samples. Sample annealed at 600 °C exhibits a higher datum of 3.37 × 10^{-13} than that of the sample annealed at 900 °C of 1.71 × 10^{-13} cm^2 s^{-1}. (e) Cyclability of the samples annealed at 600 and 900 °C at 1000 mA g^{-1} within the voltage range of 0.01–2.50 V.

Ω). This is in accordance with the tendencies in electrical conductivities (Fig. S2b†), revealing that the superior conductivity of carbon benefits the decrease in charge transfer resistance in batteries. At the same time, the Li-ion diffusion coefficient could also be calculated from the low frequencies plots of EIS spectra (Fig. 2d) based on the following equations.[29]

$$Z' = R_s + R_f + R_{ct} + \sigma_w\omega^{-1/2} \tag{3}$$

$$D_{Li^+}^{EIS} = \frac{R^2 T^2}{2A^2 n^4 F^4 C^2 \sigma_w^2} \tag{4}$$

where ω, A, n, F, C, R and T stands for the angular frequency, electrode area (0.50 cm^2), electron number (2), Faraday constant (96 500 C mol^{-1}), molar concentration of Li ions (1.0 × 10^{-3} mol cm^{-3}), gas constant (8.314 J mol^{-1} K^{-1}) and surrounding temperature (298 K), respectively. The Warburg coefficient (σ_w)

was obtained from the slopes of Z'–$\omega^{-1/2}$ curves as shown in Fig. 2d. The calculated Li-ion diffusion coefficients are 3.37 × 10^{-13} and 1.71 × 10^{-13} cm^2 s^{-1} for the samples annealed at 600 and 900 °C, respectively. Both are higher than the coefficient of commercial MnO (6.96 × 10^{-14} cm^2 s^{-1}). Combining the results of XPS, it may be concluded that cationic vacancies from Mn^{3+} in the crystal lattice leave more open void spaces for easy Li-ion diffusion.[26,28,29] However, the concentrations of cationic vacancies are approximate, as discussed above; thus, the degree of crystallinity is the other critical role for the enhanced diffusion coefficient in the sample annealed at 600 °C. The low degree in crystallinity implies a disordered arrangement in atoms and induces more void spaces as open pathways in the MnO matrix for Li-ion diffusion, as widely reported in amorphous materials.[23,50–52] The cyclability of the two samples was tested and the results are shown in Fig. 2e. Sample annealed at 600 °C has an

This journal is © The Royal Society of Chemistry 2016

J. Mater. Chem. A, 2016, **4**, 3362–3370 | **3367**

initial discharge capacity of 598 mA h g^{-1} at 1000 mA g^{-1} and the capacity increases gradually with the increase of cycles.[47] Two possible mechanisms may explain such an increase in discharge capacity; one derives from a reversible SEI effect, which suggests a pseudo-capacitive contribution from the SEI film during the process of charge and discharge.[53,54] The other may be attributed to a gradual activation of MnO in the smaller carbon channels as the battery cycles.[55] After 300 cycles, the capacity stabilizes at 650 mA h g^{-1}. However, the sample annealed at 900 °C with a high degree of crystallinity, shows an inferior cyclability as the specific capacity decreases from 431 mA h g^{-1} to 243 mA h g^{-1} within 300 cycles. Besides, the rate capabilities of all the samples are shown in Fig. S8,† and the results demonstrate that the sample annealed at 600 °C also exhibits the most competitive properties. By these comparisons, it is found that the sample with a low degree of crystallinity displays excellent cyclability at high current densities. One issue is that the sample annealed at 600 °C has a lower electrical conductivity than the sample annealed at 900 °C; however, the sample annealed at 600 °C achieved the higher specific capacity and excellent cycling stability, revealing that electrical conductivity is not the determining factor when the value exceeds a threshold. A redox reaction accompanies ion diffusion and charge transfer; thus, the electrical conductivity satisfies reactive conditions and the reaction is limited by ion diffusion. Therefore, the excellent electrochemical performance by the sample annealed at 600 °C may be attributed to the synergistic effect of cationic vacancies and disordered atom arrangements that can provide fast pathways for ion diffusion and more active sites, and reduces volume changes during phase transition.[23,50] At the same time, the three dimensional (3D) porous carbon framework guarantees fast charge transfer in the reaction.

As discussed above, the sample annealed at 600 °C possesses an excellent cyclability and a suitable discharge plateau at 0.5 V vs. Li/Li$^+$; thus, it is qualified to serve as an anode to build a high voltage capacitor. Moreover, activated carbon (AC), with a surface area of 1800 m^2 g^{-1}, was adopted as the cathode due to its sufficient surface area and chemical stability.[56] Considering the capacity match in anode and cathode, AC as cathode in half cells were tested and the rate capability is exhibited in Fig. S9.† The mass ratio was based on the charge balance of both electrodes as follows.[57,58]

$$\frac{m^+}{m^-} = \frac{C^+ \times \Delta E^+}{C^- \times \Delta E^-} \tag{5}$$

where C is specific capacitance, ΔE the potential window during the charge/discharge process and m is the mass of the electrodes. The mass ratio of the sample annealed at 600 °C and AC was calculated to be 1 : 7 on the electrodes in the Li-ion asymmetric capacitor. Fig. 3a shows the galvanostatic charge/discharge curves at various current densities, and the profiles display sloping curves that are in accordance with the characteristics of capacitors.[59,60] However, the charge–voltage curve dramatically increases initially and it is considered as a voltage jump derived from internal resistances, which also induces the same voltage decrease at the beginning of discharge process. In
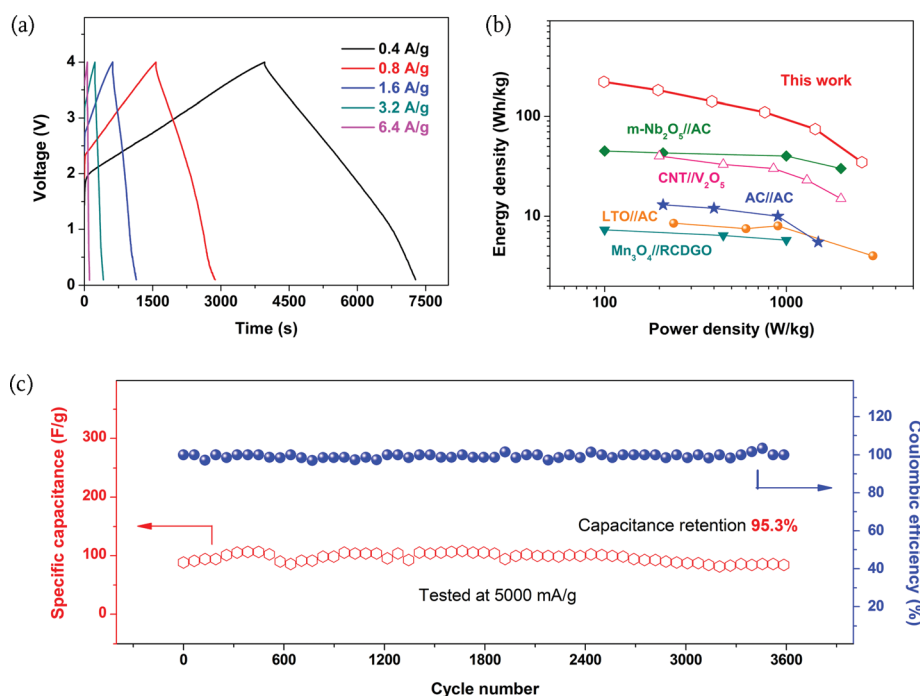

Fig. 3 (a) Galvanostatic charge/discharge profiles at various current densities in the asymmetric capacitor. (b) Ragone plot of the asymmetric capacitor based on an anode obtained with the sample annealed at 600 °C and an AC cathode. The data calculated from the total mass weight of both electrodes. The energy and power density were compared with other asymmetric systems using m-N$_{b2}$O$_5$//AC,[59] CNT//V$_2$O$_5$,[67] AC//AC[66] and LTO//AC[70] in Li-ion electrolytes, and Mn$_3$O$_4$//RCDGO[65] in an aqueous solution. (c) Cyclability of the asymmetric capacitor with a tested current density of 5000 mA g^{-1} and the capacitance are retained at the initial level without visible degradation within 3600 cycles.

fact, there is a more slight voltage decrease than the speculated one, implying that the decrease is also due to another reason. The large surface area might offer a reasonable indication. Based on the specific double-layer capacitance of 0.08–0.18 F m^{-2},[61,62] this porous sample can achieve a theoretical specific capacitance of 18–36 F g^{-1}. The voltage curve rises to 2.0 V within 150 s, and suggests that the achieved specific capacitance is $\sim$30 F g^{-1}. Thus, it can be concluded that the EDLC effect from the surface area of the sample causes a special phenomenon at the initial charge curve in the full capacitor. Besides, the Ragone plot exhibits the energy and power density of the capacitor and compares it with the reported systems (Fig. 3b). Capacitors with organic electrolytes deliver higher energy density compared with aqueous capacitors at the same power density because of the wide working voltage window achievable in organic systems,[63,64] such as the Mn_3O_4//RCDGO capacitor with a low energy density.[65] Moreover, the organic systems built on different materials also perform discrepant properties, for example, the AC//AC system delivers an energy density of 10 W h kg^{-1} at a power density of $\sim$1000 W kg^{-1},[66] but the system made of CNT and V_2O_5 can display a power density of $\sim$30 W h kg^{-1} at the same power density,[67] indicating that the anode based on oxides enhances the energy density in organic systems. The Li-ion capacitor fabricated with the sample annealed at 600 °C and AC achieved the maximum energy and power density of 220 W h kg^{-1} and 2608 W kg^{-1}, respectively, which has competitive strength compared with other systems because of the reasonable plateau in the electrochemical potential and high capacity as characterized above. The capacitor was cycled at 5000 mA g^{-1} with 3600 cycles and the capacitance retention was 95.3% (Fig. 3c). It exhibits an excellent cycling stability compared with those in the reported literature.[68,69] For example, the $H_2Ti_2O_{13}$//CMK-3 Li-ion capacitor when subjected to 1000 cycles at 1.5 A g^{-1} in the voltage window of 0–3.5 V, the capacitance retained was 80% of the initial value.[68] From the above discussions, it can be concluded that the spindle-like carbon encapsulated MnO with a low degree crystallinity exhibits excellent stability in the half cell and as a Li-ion capacitor. More importantly, the Li-ion capacitor achieved high energy and power density synchronously, demonstrating a competitive potential in commercial devices for powering portable electronic apparatus and electric vehicles.

Conclusions

Spindle-like porous carbon dispersed MnO nanocrystals were synthesized through the hydrothermal method and cationic vacancies were introduced by the incomplete reduction of high valence state Mn(III). A moderate calcination temperature of 600 °C was found to be effective for the fabrication of samples with a low degree of crystallinity. This benefits the phase transition in conversion reactions and the porous carbon matrix further facilitates charge transfer and penetration of electrolyte into the material. The synergistic combination of these three factors endows the resulting samples with enhanced capacity and cyclability. The Li-ion pseudo-capacitor with the spindle MnO as an anode and AC as a cathode offers a significantly high energy density of 220 W h kg^{-1}, comparable to that of Li-ion batteries, with little degradation over 3600 cycles.

Acknowledgements

Notes and references

1 J.-M. Tarascon; and P. Simon, *Electrochemical Energy Storage*, John Wiley & Sons, Inc., 2015.

2 C. Liu, F. Li, L.-P. Ma and H.-M. Cheng, *Adv. Mater.*, 2010, **22**, E28–E62.

3 D. Larcher and J. M. Tarascon, *Nat. Chem.*, 2015, **7**, 19–29.

4 K. Li, H. Bian, C. Liu, D. Zhang and Y. Yang, *Renewable Sustainable Energy Rev.*, 2015, **42**, 1464–1474.

5 R. Singh and A. D. Setiawan, *Renewable Sustainable Energy Rev.*, 2013, **22**, 332–345.

6 Y. K. a. J. C. H. H. D. Abrun, *Phys. Today*, 2008, **61**, 43–47.

7 B. Dunn, H. Kamath and J.-M. Tarascon, *Science*, 2011, **334**, 928–935.

8 M. Armand and J. M. Tarascon, *Nature*, 2008, **451**, 652–657.

9 J. B. Goodenough, *Energy Environ. Sci.*, 2014, **7**, 14.

10 J. R. Miller and P. Simon, *Science*, 2008, **321**, 651–652.

11 P. Simon, Y. Gogotsi and B. Dunn, *Science*, 2014, **343**, 1210–1211.

12 J. Yan, Q. Wang, T. Wei and Z. Fan, *Adv. Energy Mater.*, 2014, **4**, 1300816.

13 V. Augustyn, P. Simon and B. Dunn, *Energy Environ. Sci.*, 2014, **7**, 1597–1614.

14 V. Aravindan, J. Gnanaraj, Y.-S. Lee and S. Madhavi, *Chem. Rev.*, 2014, **23**, 11619–11635.

15 Y. Deng, L. Wan, Y. Xie, X. Qin and G. Chen, *RSC Adv.*, 2014, **4**, 23914–23935.

16 H. Jiang, Y. Hu, S. Guo, C. Yan, P. S. Lee and C. Li, *ACS Nano*, 2014, **8**, 6038–6046.

17 Y. K. Peng, C. W. Lai, C. L. Liu, H. C. Chen, Y. H. Hsiao, W. L. Liu, K. C. Tang, Y. Chi, J. K. Hsiao, K. E. Lim, H. E. Liao, J. J. Shyue and P. T. Chou, *ACS Nano*, 2011, **5**, 4177–4187.

18 Y. Xia, Z. Xiao, X. Dou, H. Huang, X. H. Lu, R. J. Yan, Y. P. Gan, W. J. Zhu, J. P. Tu, W. K. Zhang and X. Y. Tao, *ACS Nano*, 2013, **7**, 7083–7092.

19 W.-M. Chen, L. Qie, Y. Shen, Y.-M. Sun, L.-X. Yuan, X.-L. Hu, W.-X. Zhang and Y.-H. Huang, *Nano Energy*, 2013, **2**, 412–418.

20 S. Zhang, L. Zhu, H. Song, X. Chen and J. Zhou, *Nano Energy*, 2014, **10**, 172–180.

21 E. Uchaker and G. Cao, *Chem.–Asian J.*, 2015, **10**, 1608–1617.

22 Y. Idota, T. Kubota, A. Matsufuji, Y. Maekawa and T. Miyasaka, *Science*, 1997, **276**, 1395–1397.

23 O. B. Chae, J. Kim, I. Park, H. Jeong, J. H. Ku, J. H. Ryu, K. Kang and S. M. Oh, *Chem. Mater.*, 2014, **26**, 5874–5881.

24 J. Liu, J. Xu, K. Zhou, L. Wang and X. Wei, *RSC Adv.*, 2015, **5**, 34088–34093.

25 J. Nai, J. Kang and L. Guo, *Sci. China Mater.*, 2015, **58**, 44–59.

26 D. Liu, Y. Liu, B. B. Garcia, Q. Zhang, A. Pan, Y.-H. Jeong and G. Cao, *J. Mater. Chem.*, 2009, **19**, 8789–8795.

27 B. P. Hahn, J. W. Long and D. R. Rolison, *Acc. Chem. Res.*, 2013, **46**, 1181–1191.

28 B. P. Hahn, J. W. Long, A. N. Mansour, K. A. Pettigrew, M. S. Osofsky and D. R. Rolison, *Energy Environ. Sci.*, 2011, **4**, 1495.

29 H. Song, Y. Liu, C. Zhang, C. Liu and G. Cao, *J. Mater. Chem. A*, 2015, **3**, 3547–3558.

30 N. Li, K. Du, G. Liu, Y. Xie, G. Zhou, J. Zhu, F. Li and H. M. Cheng, *J. Mater. Chem. A*, 2013, **1**, 1536–1539.

31 C. Liu, H. Song, C. Zhang, Y. Liu, C. Zhang, X. Nan and G. Cao, *Nano Res.*, 2015, **8**, 3372–3383.

32 A. Guinier, *X-Ray Diffraction: In Crystals, Imperfect Crystals, and Amorphous Bodies*, Dover Publications, 1994.

33 Y. Zhou, S. L. Candelaria, Q. Liu, E. Uchaker and G. Cao, *Nano Energy*, 2015, **12**, 567–577.

34 M. A. Pimenta, G. Dresselhaus, M. S. Dresselhaus, L. G. Cancado, A. Jorio and R. Saito, *Phys. Chem. Chem. Phys.*, 2007, **9**, 1276–1290.

35 L. F. Shen, H. S. Li, E. Uchaker, X. G. Zhang and G. Z. Cao, *Nano Lett.*, 2012, **12**, 5673–5678.

36 C. Zhang, H. Song, C. Liu, Y. Liu, C. Zhang, X. Nan and G. Cao, *Adv. Funct. Mater.*, 2015, **25**, 3497–3504.

37 Y. Sun, X. Hu, W. Luo and Y. Huang, *J. Mater. Chem.*, 2012, **22**, 19190–19195.

38 B. J. Tan, K. J. Klabunde and P. M. A. Sherwood, *J. Am. Chem. Soc.*, 1991, **113**, 855–861.

39 V. Di Castro and G. Polzonetti, *J. Electron Spectrosc. Relat. Phenom.*, 1989, **48**, 117–123.

40 R. Dong, Q. Ye, L. Kuang, X. Lu, Y. Zhang, X. Zhang, G. Tan, Y. Wen and F. Wang, *ACS Appl. Mater. Interfaces*, 2013, **5**, 9508–9516.

41 G. Xie, L. Yu and Y. Liu, in *Series in Inorganic Chemistry*, ed. Q. Zhang, Science Press, 2012, vol. IX, p. 4.

42 S.-J. L. Kang, *Sintering: Densification, Grain Growth and Microstructure*, A Butterworth-Heinemann Title, 2005.

43 R.-Q. Song and H. Cölfen, *Adv. Mater.*, 2010, **22**, 1301–1330.

44 E. Uchaker and G. Cao, *Nano Today*, 2014, **9**, 499–524.

45 Z. Hong, M. Wei, T. Lan and G. Cao, *Nano Energy*, 2012, **1**, 466–471.

46 M. Inagaki, Y. Hirose, T. Matsunaga, T. Tsumura and M. Toyoda, *Carbon*, 2003, **41**, 2619–2624.

47 Z. Cai, L. Xu, M. Yan, C. Han, L. He, K. M. Hercule, C. Niu, Z. Yuan, W. Xu, L. Qu, K. Zhao and L. Mai, *Nano Lett.*, 2015, **15**, 738–744.

48 H. Jiang, Y. J. Hu, S. J. Guo, C. Y. Yan, P. S. Lee and C. Z. Li, *ACS Nano*, 2014, **8**, 6038–6046.

49 J. Wang, J. Polleux, J. Lim and B. Dunn, *J. Phys. Chem. C*, 2007, **111**, 14925–14931.

50 E. Uchaker, Y. Z. Zheng, S. Li, S. L. Candelaria, S. Hu and G. Z. Cao, *J. Mater. Chem. A*, 2014, **2**, 18208–18214.

51 Y. Liu, Y. Xu, X. Han, C. Pellegrinelli, Y. Zhu, H. Zhu, J. Wan, A. C. Chung, O. Vaaland, C. Wang and L. Hu, *Nano Lett.*, 2012, **12**, 5664–5668.

52 Y. Fang, L. Xiao, J. Qian, X. Ai, H. Yang and Y. Cao, *Nano Lett.*, 2014, **14**, 3539–3543.

53 A. Ponrouch, P.-L. Taberna, P. Simon and M. R. Palacín, *Electrochim. Acta*, 2012, **61**, 13–18.

54 S. Laruelle, S. Grugeon, P. Poizot, M. Dollé, L. Dupont and J.-M. Tarascon, *J. Electrochem. Soc.*, 2002, **149**, A627–A634.

55 Z. Li, J. T. Zhang, Y. M. Chen, J. Li and X. W. Lou, *Nat. Commun.*, 2015, **6**, 8850.

56 M. Sevilla and R. Mokaya, *Energy Environ. Sci.*, 2014, **7**, 1250.

57 J. Chang, M. Jin, F. Yao, T. H. Kim, V. T. Le, H. Yue, F. Gunes, B. Li, A. Ghosh, S. Xie and Y. H. Lee, *Adv. Funct. Mater.*, 2013, **23**, 5074–5083.

58 Z. Fan, J. Yan, T. Wei, L. Zhi, G. Ning, T. Li and F. Wei, *Adv. Funct. Mater.*, 2011, **21**, 2366–2375.

59 E. Lim, H. Kim, C. Jo, J. Chun, K. Ku, S. Kim, H. I. Lee, I.-S. Nam, S. Yoon, K. Kang and J. Lee, *ACS Nano*, 2014, **8**, 8968–8978.

60 M. Yang, Y. Zhong, J. Ren, X. Zhou, J. Wei and Z. Zhou, *Adv. Energy Mater.*, 2015, 1500550.

61 D. Lozano-Castelló, D. Cazorla-Amorós, A. Linares-Solano, S. Shiraishi, H. Kurihara and A. Oya, *Carbon*, 2003, **41**, 1765–1775.

62 L. Wang, M. Fujita and M. Inagaki, *Electrochim. Acta*, 2006, **51**, 4096–4102.

63 J. Yang, C. Yu, X. Fan, C. Zhao and J. Qiu, *Adv. Funct. Mater.*, 2015, **25**, 2109–2116.

64 Z. Weng, F. Li, D. W. Wang, L. Wen and H. M. Cheng, *Angew. Chem., Int. Ed.*, 2013, **52**, 3722–3725.

65 F. Gao, J. Qu, Z. Zhao, Q. Zhou, B. Li and J. Qiu, *Carbon*, 2014, **80**, 640–650.

66 A. Du Pasquier, I. Plitz, S. Menocal and G. Amatucci, *J. Power Sources*, 2003, **115**, 171–178.

67 Z. Chen, V. Augustyn, J. Wen, Y. Zhang, M. Shen, B. Dunn and Y. Lu, *Adv. Mater.*, 2011, **23**, 791–795.

68 Y. Wang, Z. Hong, M. Wei and Y. Xia, *Adv. Funct. Mater.*, 2012, **22**, 5185–5193.

69 V. Aravindan, W. Chuiling, M. V. Reddy, G. V. Rao, B. V. Chowdari and S. Madhavi, *Phys. Chem. Chem. Phys.*, 2012, **14**, 5808–5814.

70 V. Ruiz, C. Blanco, R. Santamaría, J. M. Ramos-Fernández, M. Martínez-Escandell, A. Sepúlveda-Escribano and F. Rodríguez-Reinoso, *Carbon*, 2009, **47**, 195–200.